

This is a self-archived version of an original article. This version may differ from the original in pagination and typographic details.

Author(s): Malola, Sami; Kaappa, Sami; Häkkinen, Hannu

Title: The Role of Nanocrystal Symmetry in the Crossover Region from Molecular to Metallic Gold Nanoparticles

Year: 2019

Version: Accepted version (Final draft)

Copyright: © 2019 American Chemical Society.

Rights: In Copyright

Rights url: <http://rightsstatements.org/page/InC/1.0/?language=en>

Please cite the original version:

Malola, S., Kaappa, S., & Häkkinen, H. (2019). The Role of Nanocrystal Symmetry in the Crossover Region from Molecular to Metallic Gold Nanoparticles. *Journal of Physical Chemistry C*, 123(33), 20655-20663. <https://doi.org/10.1021/acs.jpcc.9b05863>



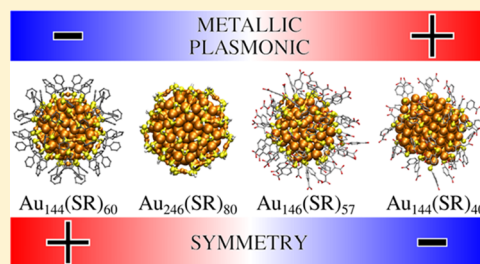
Role of Nanocrystal Symmetry in the Crossover Region from Molecular to Metallic Gold Nanoparticles

Sami Malola,[†] Sami Kaappa,[†] and Hannu Häkkinen^{*,†,‡,§}

[†]Department of Physics, Nanoscience Center and [‡]Department of Chemistry, Nanoscience Center, University of Jyväskylä, Jyväskylä FI-40014, Finland

Supporting Information

ABSTRACT: There is a widespread interest to design ambient-stable gold nanoparticles with tailored physicochemical properties for applications in several areas such as plasmonics, nanomedicine, catalysis, biological imaging, sensing, and nanoelectronics. It has been known for a long time that optical response of gold nanoparticles changes drastically in a crossover region from 150 to 250 gold atoms, from a “molecule-like” to “metallic” behavior, but insufficient knowledge of atomic structures has precluded detailed computational studies on the underlying mechanisms. Here, we analyze the electronic structure and optical and chiroptical properties of recently reported gold nanoparticles of 144, 146, and 246 gold atoms that are made by wet chemistry methods and whose structures have been resolved to atomic precision. We demonstrate computationally how regrouping of the quantum states of valence electrons can affect drastically the optical properties of nanoparticles in the crossover-size region, by either generating a multiband molecule-like or a monotonous “plasmon-like” or metallic optical absorption. The lower the symmetry of the gold core, the more metallic is the nanoparticle. The underlying mechanism arises from symmetry-sensitive distribution of the electronic levels of the nanoparticle close to Fermi energy.



INTRODUCTION

Gold nanoparticles are widely investigated for various applications in nanotechnology in areas such as plasmonics, nanomedicine, catalysis, biological imaging, sensing, and nanoelectronics.^{1–3} Although it has been known since Faraday’s times that gold can be dispersed in colloidal solutions as fine nanometer-size particles that display a fascinating spectrum of colors,⁴ it is only during the last decade that detailed investigations into the structure–property relationship of gold nanoparticles have been made possible by great advances in synthesis, purification, and characterization of specific compounds with molecular formula Au_xL_y , where L is the protecting ligand molecule, usually thiolate, phosphine, halide, or alkynyl.⁵ These nanoparticles are often called “monolayer-protected clusters” (MPCs) since their total structure, including that of the ligand layer, can be solved to atomic precision by X-ray diffraction from samples where the clusters have formed high-quality single crystals. The largest currently known gold-based MPCs with precise atomistic structures have close to 300 gold atoms and metal diameters of close to 3 nm.^{6–8}

Bulk gold is a simple monovalent s-metal and a good electric and thermal conductor. Confining the electrons in the delocalized $Au(6s)$ -derived conduction band of bulk gold into a nanometer-size volume causes discretization of the electron states into a shell structure whose details depend on the size, shape, and point group symmetry of the confining gold nanocrystal. These strong finite-size effects have for long been recognized to be an important factor in defining many

physicochemical properties of both bare and ligand-protected gold nanoclusters.^{9–13} Of special interest is the energy gap that can form at the Fermi level. Simple considerations following ideas of Fröhlich¹⁴ and Kubo¹⁵ show that a three-dimensional electron gas confined in a volume V with N electrons has a density of states (DOS) D at Fermi level E_F such that $D(E_F) = 3N/2E_F$.^{12,16} Thus, an average value of the energy gap Δ at the Fermi level is $\Delta(E_F) = 1/D(E_F) = 2E_F/3N$. The existence and value of $\Delta(E_F)$ is relevant for considerations of the onset size for the “metallic” behavior of gold nanoparticles, manifested, e.g., by appearance of the surface plasmon resonance (SPR) or metallic electrochemical charging and redox properties. At room temperature, thermal excitations of electrons over the $\Delta(E_F)$ become relevant when $\Delta(E_F) \approx 25$ meV. Taking into account the Fermi energy of gold (5.5 eV), this leads to the onset size of 147 gold atoms and a spherical diameter of 1.7 nm.¹² One has to note that this average result is however strongly modified by the details of the electron shell structure which makes the level spacing highly nonuniform and can change the magnitude and location of Δ close to E_F .

Interestingly, it has been known since the late 1990s that ambient-stable thiol-protected gold nanoparticles of size very close to the above-mentioned onset can indeed be abundantly synthesized in both organic and aqueous solvents.¹⁷ First, they were referred to as “29 kDa” particles based on the

Received: June 19, 2019

Revised: July 30, 2019

Published: July 30, 2019

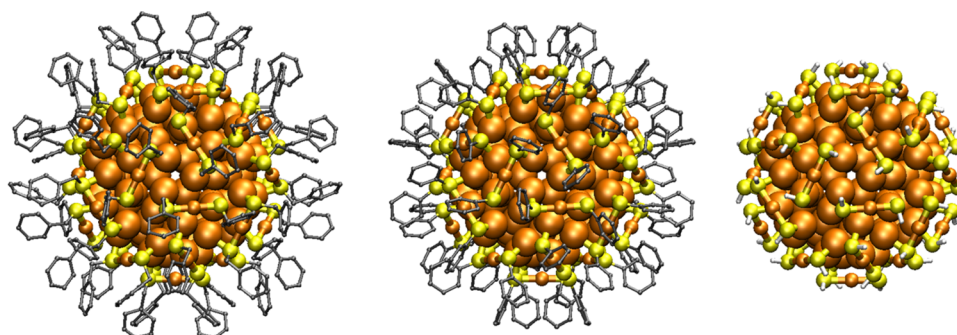


Figure 1. Structures of the $\text{Au}_{144}(\text{SR})_{60}$ nanoparticles considered in this work. Left: experimental structure of $\text{Au}_{144}(\text{SCH}_2\text{Ph})_{60}$,³⁹ center and right: simplified models based on the experimental structure but with ligands SPh (center) and SH (right). Au: orange, S: yellow, C: gray, H: white.

approximate molecular mass. Refined mass measurements yielded first assignments for molecular formula as $\text{Au}_{144}(\text{SR})_{59}$,¹⁸ $\text{Au}_{144}(\text{SR})_{60}$,¹⁹ and $\text{Au}_{144-146}(\text{SR})_{59-60}$.²⁰ Their optical and electrochemical properties have since been extensively experimentally studied, and computational models have been built for calculations of their electronic structure and optical properties.^{21–38} The optical properties of these nanoparticles are known to indicate “nonmetallic” behavior (i.e., absence of the SPR peak but exhibiting instead several absorption bands),^{18–20,22,25–29} but, on the other hand, electrochemical charging properties at room temperature indicate absence of $\Delta(E_F)$ and show an evenly spaced, multiple series of reduction–oxidation states^{22–24} indicating a metallic behavior. Furthermore, the optical absorption spectra are known to be sensitive to temperature;^{28,29} to some extent, to the nature of the ligand layer,^{36–38} and to the elemental composition of the metal core, i.e., intermetallic $\text{Au}_{144-x}\text{Ag}_x(\text{SR})_{60}$ ^{31–33} and $\text{Au}_{144-x}\text{Cu}_x(\text{SR})_{60}$ ^{34,35} particles show UV–visible absorption markedly different from that of the pure-gold particle.

A theoretical model for this nanoparticle was presented concurrently with the first accurate mass spectrometry data in 2009 as the first prediction of the atomic structure of $\text{Au}_{144}(\text{SR})_{60}$ by Lopez-Acevedo et al.²¹ In that model, the gold core was built from concentric Mackay icosahedral 12- and 42-atom shells completed by an anti-Mackay shell of 60 gold atoms. This 114-atom structure was covered by 30 RS–Au–SR units (Supporting Information, Figure S1). The arrangement of these units makes the overall $\text{Au}_{144}\text{S}_{60}$ framework of chiral icosahedral (*I*) symmetry that is also reflected in the slightly chiral arrangements of the 60-atom anti-Mackay shell at the metal–ligand interface (Figure S1 in the Supporting Information; the closest nonchiral structure of the 60-atom layer would be I_h rhombicosi-dodecahedron). Calculations based on the density functional theory (DFT) showed that this model gave an excellent agreement in comparison to the computed powder X-ray diffraction function to the experimentally measured one,¹⁷ predicted a distinct electronic shell structure around E_F giving the lowest allowed optical transitions in the midinfrared, and indicated a metallic charging in electrochemistry as known at the time.^{22–24} The absence of the central atom was argued by considerations to relieve built up strain in the icosahedral metal structure. All of the later computational work by others has been based on this model with refinements regarding the symmetry of the organic part of the ligand layer^{29,30} and occupation of the metal sites for modeling Au–Ag or Au–Cu 144-atom particles.^{32,33,35}

The emergence of the definite experimental structure of $\text{Au}_{144}(\text{SR})_{60}$ (with SR = phenyl methyl thiolate, SCH_2Ph) from the single-crystal X-ray diffraction in 2018³⁹ gives now firm grounds to analyze the structure–property relations of this nanoparticle (Figure 1). The experimental structure directly confirms the predicted chiral icosahedral *I*– $\text{Au}_{144}\text{S}_{60}$ framework structure by Lopez-Acevedo et al.²¹ and allows now detailed DFT-based analyses of the interplay between symmetry, electronic structure, optical absorption, and circular dichroism (CD). We show here that the choice of the organic ligand has a minor effect on the electronic shell structure of the metal core and on the UV–visible absorption as long as the overall point group symmetry of the nanoparticle remains the same. By comparing to two other recently atomically defined nanoparticles of similar size, namely, C_{2v} – $\text{Au}_{146}(\text{SR})_{57}$ ⁴⁰ and C_1 – $\text{Au}_{144}(\text{SR})_{40}$,^{41,42} we show that lowering of the symmetry changes drastically the electronic shell structure around E_F leading to a more uniform density of electron states, more featureless UV–visible absorption, and emergence of a weak plasmon-like absorption band. Further comparisons to the atom-precise D_5 -symmetric nanoparticle $\text{Au}_{246}(\text{SR})_{80}$ ⁶ show the drastic role of the high point group symmetry leading to a distinct shell structure and nonplasmonic absorption of this larger particle, not examined before by DFT calculations. The decisive role of the point group symmetry of the metal core and its effects on the electronic shell structure of gold nanoparticles close to the onset of metallic behavior have not been clearly demonstrated before. This discussion is of fundamental interest since it sheds light on mechanisms of how “molecular” nanoparticle properties can change to metallic and is of practical interest since understanding these mechanisms helps design ambient-stable nanoparticles for applications.

METHODS

All of the electronic structure calculations were done by using the real-space grid-based DFT package GPAW.⁴³ We used the Perdew–Burke–Ernzerhof (PBE) exchange–correlation functional⁴⁴ and 0.2 Å grid spacing for wave functions and densities. The optimization was stopped when the residual forces were below 0.05 eV/Å. The GPAW projector setups include scalar-relativistic effects for gold. We analyzed the electronic shell structure of the nanoparticles in two ways: by projecting the electron density in the Kohn–Sham orbitals to either spherical harmonics¹¹ or point group (I_h) symmetry representations as described elsewhere.⁴⁵ Linear optical absorption and circular dichroism (CD) spectra were calculated by using the linear-response time-dependent DFT

(LR-TDDFT) module in GPAW.⁴⁶ PBE functional was used for electron–electron interactions, and the electron wave functions and densities were treated in a real-space grid with a spacing of 0.25 Å. Decomposition of a selected number of optical transitions into single electron–hole (e–h) excitations in Kohn–Sham basis was done in the framework of the density functional perturbation theory by using the so-called transition contribution map (TCM) method^{47,48} with transition dipole contributions shown (DTCM). CD spectra were analyzed by decomposing the e–h contributions to the rotatory strengths rotational transition contribution maps (RTCM) including both the transition dipole moment and magnetic moment (see the Supporting Information of ref 48). Both DTCM and RTCM analyses are convenient and flexible tools to decompose contributions to linear and CD absorption by multiple ways, e.g., by classifying the e–h pairs according to global symmetries (approximate angular momenta or point group representations), local symmetries near the atoms (corresponding to analysis by “atomic orbitals”), atom types, or spatial regions of the nanoparticle (metal core, atom shell, ligand layer).

To compare our results between the highly symmetric $\text{Au}_{144}(\text{SR})_{60}$ and recently reported lower-symmetry particles of similar size, namely, $\text{C}_{2v}\text{-Au}_{146}(\text{SR})_{57}$ ⁴⁰ and $\text{C}_1\text{-Au}_{144}(\text{SR})_{40}$,^{41,42} we analyzed the electronic structure and linear absorption spectra of these compounds using the published structural information. The $\text{C}_{2v}\text{-Au}_{146}(\text{SR})_{57}$ particle was analyzed in a trianionic form using the experimental atomic coordinates from the work of Vergara et al.⁴⁰ The atomic structure of $\text{C}_1\text{-Au}_{144}(\text{SR})_{40}$ is based on our earlier work⁴² where the structure of the Au_{144} core is taken from the electron microscopy data of Azubel et al.⁴¹ and the ligand layer has been built around the core as explained in ref 42. The electronic structure and optical absorption of a larger but still rather symmetric (D_5) $\text{Au}_{246}(\text{SR})_{80}$ particle was analyzed as well, based on the published X-ray structure⁶ of $\text{Au}_{246}(\text{SPhCH}_3)_{80}$ from which a simplified $\text{Au}_{246}(\text{SH})_{80}$ model was built by fixing the Au–S framework to the experimental structure and optimizing all 80 S–H bonds.

RESULTS

I_h Symmetry and the Electronic Structure of $\text{Au}_{144}(\text{SR})_{60}$. Our comparative analysis is based on the experimental X-ray structure³⁹ of $\text{Au}_{144}(\text{SCH}_2\text{Ph})_{60}$ and two structures derived from it (Figure 1). By keeping the heavy atoms Au and S in places determined by the experimental structure, we made two additional structures where the sulfurs are passivated either by a phenyl group or hydrogen. The S–C bonds and the phenyl structure in the former case and the S–H bonds in the latter case were optimized using the real-space grid-based DFT package GPAW⁴³ as explained in Methods. Although the proper symmetry group for the thiol-protected $\text{Au}_{144}(\text{SR})_{60}$ nanoparticle (Figure 1) is the chiral icosahedral (I) group, it is instructive to analyze the electronic structure in the context of the I_h group. Selecting this symmetry group is also justified by the fact that we found all frontier orbitals (orbitals that lie in the range from 1 eV below to 2 eV above of the Fermi energy) to be described by very high weights (typically 80–90%) by representations belonging to I_h symmetry class. The number of electrons in delocalized orbitals of this nanoparticle, originating mainly from Au(6s) electrons, is 84 by taking into account the electron-withdrawing nature of the 60 thiolates ($144 - 60 = 84$).¹¹ The

spherical harmonics analysis shows the presence of 1G, 1H, 2D, 3S, 1I, 2F, 1J, and 3P symmetries, corresponding qualitatively to the spherical electron gas model⁴⁹ (Figure 2,

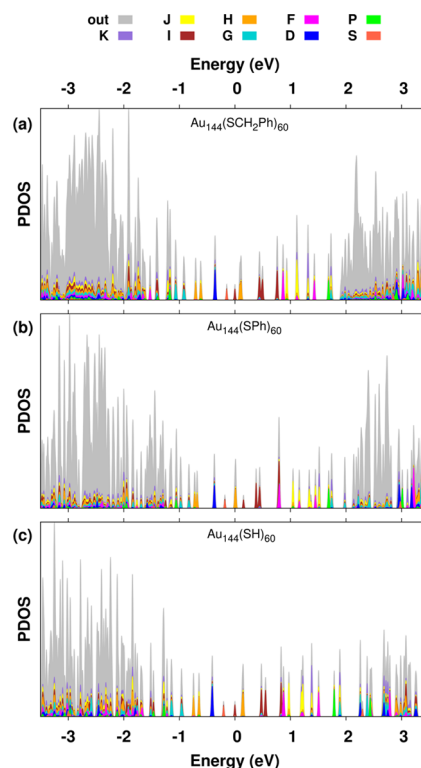


Figure 2. Projection of the density of electron states (PDOS) to spherical harmonics for Kohn–Sham orbitals in the vicinity of the Fermi energy ($E = 0$) for (a) $\text{Au}_{144}(\text{SCH}_2\text{Ph})_{60}$, (b) $\text{Au}_{144}(\text{SPh})_{60}$, and (c) $\text{Au}_{144}(\text{SH})_{60}$. Each of the states is broadened with a 0.01 eV Gaussian.

cf. a similar analysis was first done by Lopez-Acevedo et al.²¹). One may note that although the above-mentioned shells span electron numbers up to a high count of 168, their energy ordering deviates from the exactly spherical three-dimensional electron gas model as expected.⁴⁹ Figure 3 gives the I_h -projected symmetries of the $\text{Au}_{144}(\text{SR})_{60}$ nanoparticles protected by SH and SCH_2Ph ligands. The following observations can be made by comparing Figures 2 and 3: (i) the sequence of the subshells with I_h symmetries is exactly the same in both systems for orbitals in the energy region of $-1 < E_f < 2$ eV, (ii) particularly the 1H(22) symmetric shell (Figure

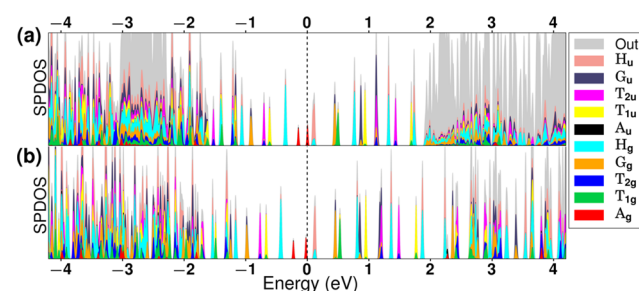


Figure 3. I_h symmetry-projected electron density of states (SPDOS) for (a) $\text{Au}_{144}(\text{SCH}_2\text{Ph})_{60}$ and (b) $\text{Au}_{144}(\text{SH})_{60}$ in the vicinity of the Fermi energy ($E = 0$). Each of the states is broadened with a 0.01 eV Gaussian.

2) is strongly split below and above E_f into $T_{2u}(6)$, $T_{1u}(6)$, and $H_u(10)$ subshells, where the electron occupations are shown in parentheses, and (iii) in most cases, the intershell energy gaps are very much independent of the system. Significant deviations in the electronic structure between the SH- and SCH_2Ph -protected particles are seen in the energy regions of $-3 \text{ eV} < \epsilon < -2 \text{ eV}$ and $\epsilon > 2 \text{ eV}$ states due to the existence of the occupied and unoccupied π -electron states of the phenyl ring in the SCH_2Ph -protected particle. Due to the similarity of the Kohn–Sham electronic structure between these nanoparticles, optical absorption in the UV–visible region can also be expected to be rather similar, as we will next discuss in detail.

Linear Optical Absorption. Figure 4 compares the linear absorption spectra of the SH-, SPh-, and SCH_2Ph -protected

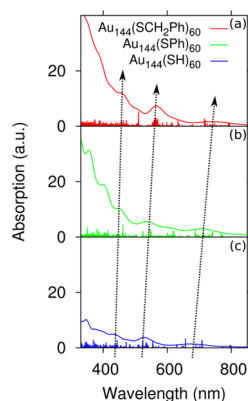


Figure 4. Computed linear optical absorption spectra of (a) $\text{Au}_{144}(\text{SCH}_2\text{Ph})_{60}$, (b) $\text{Au}_{144}(\text{SPh})_{60}$, and (c) $\text{Au}_{144}(\text{SH})_{60}$. The individual optical lines (marked by sticks) are broadened by 0.075 eV Gaussians for the continuous curves. The red shifts of the lowest three absorption peaks are shown by the dotted arrows.

Au_{144} nanoparticles as computed by the linear-response time-dependent DFT (LR-TDDFT) method (see Methods). Interestingly, all three spectra show very similar features in the visible region; only a systematic red shift is observed when going from $\text{Au}_{144}(\text{SH})_{60}$ to $\text{Au}_{144}(\text{SCH}_2\text{Ph})_{60}$ (674 to 738, 530 to 566, and 434 to 461 nm for the first three clear low-energy peaks, as marked by the arrows in Figure 4). This almost constant red shift in the peak energies (0.14–0.16 eV) can be qualitatively understood while examining the radially averaged Kohn–Sham all-electron potential (Figure 5). One can see that the potential in the gold core including the Au–S layer, that is, in the $\text{Au}_{144}\text{S}_{60}$ moiety (first four minima), is very much unaffected by the nature of the ligand layer, but the extent of SPh and SCH_2Ph ligands smoothens the potential for radial distances $> 9 \text{ \AA}$ compared to the SH-protected particle, thus allowing a spill-out of the electrons in the metal core to the ligand layer. This decreases the average electron density in the gold core inducing the observed red shift of the absorption peaks by arguments from the simple Drude model of plasmons in electron gas.

A more detailed analysis of three marked peaks (Figure 4a) in the absorption spectrum of $\text{Au}_{144}(\text{SCH}_2\text{Ph})_{60}$ is shown in Figure 6 in terms of the dipole transition contribution maps (DTCMs). The electronic density of states is expressed in two ways, projecting either to the I_h symmetry representations (SPDOS) or to local atomic orbitals (APDOS). The diagonal dashed line shows the condition where electron–hole energy

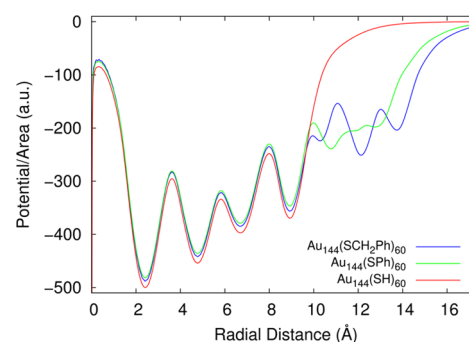


Figure 5. Radially averaged total single-particle Kohn–Sham potential for $\text{Au}_{144}(\text{SH})_{60}$, $\text{Au}_{144}(\text{SPh})_{60}$, and $\text{Au}_{144}(\text{SCH}_2\text{Ph})_{60}$. Note that the maximum of the potential at the origin is due to the atom vacancy at the center of the metal core.

difference equals the absorption energy, i.e., $\epsilon_e - \epsilon_h = hc/\lambda$. It can be clearly seen that all e–h contributions with $\epsilon_e - \epsilon_h < hc/\lambda$ contribute constructively to the transition dipole moment while all e–h contributions with $\epsilon_e - \epsilon_h > hc/\lambda$ contribute destructively screening the dipole moment. Up to the 461 nm (2.7 eV) peak, the absorption is dominantly determined by the atomic Au(sp), Au(d), and S(p) states, while the π -electrons in the phenyl ring of the ligand do not contribute. This also explains why the absorption spectra in Figure 4 are very similar for all of the three considered systems in the area where $\lambda > 400 \text{ nm}$, confirmed also by the DTCM analysis of the $\text{Au}_{144}(\text{SH})_{60}$ particle shown in Figure S2. The differences in the ligand layer become dominating for shorter wavelengths where the π -electrons contribute.

Circular Dichroism. As discussed in Introduction, the structural prediction for $\text{Au}_{144}(\text{SR})_{60}$ by Lopez-Acevedo et al.²¹ implies chirality in the system. As Figure S1 shows in detail, the underlying nonchiral I_h rhombicosi-dodecahedron (an Archimedean solid) has 30 square facets that are then distorted by bonding of the 30 RS–Au–SR diagonally on top of each facet. The bonding direction determines the handedness of the chiral structure when examined locally around each of the 12 C_5 axes. In addition, all sulfurs are intrinsically chiral centers since the electronic bonding environment at each sulfur has four nonequivalent directions.⁵⁰ We have previously predicted from computations that all particles based on the predicted $\text{Au}_{144}(\text{SR})_{60}$ structure²¹ should have detectable CD signal in the UV–visible region.³³ A comparison of the computed CD absorption spectrum between the experimental $\text{Au}_{144}(\text{SCH}_2\text{Ph})_{60}$ particle, its SH-derived model, and the previously well-characterized chiral $\text{Au}_{38}(\text{SCH}_2\text{CH}_2\text{Ph})_{24}$ nanoparticle is shown in Figure 7. In line with the comparison for linear absorption, the CD signals for $\text{Au}_{144}(\text{SCH}_2\text{Ph})_{60}$ and $\text{Au}_{144}(\text{SH})_{60}$ are very similar in the region $\lambda > 400 \text{ nm}$ but have distinct differences in the range of 300–400 nm due to the different ligand layer. Altogether, 14 maxima (+) or minima (–) can be seen in the CD spectrum of $\text{Au}_{144}(\text{SCH}_2\text{Ph})_{60}$. The strongest peaks are about 10 times stronger than the peaks in the CD spectrum computed for the $\text{Au}_{38}(\text{SCH}_2\text{CH}_2\text{Ph})_{24}$ particle^{51,52} using its experimental structure.^{53,54}

Analysis of the rotational transition contribution maps (RTCM) for three selected CD signals of $\text{Au}_{144}(\text{SCH}_2\text{Ph})_{60}$ at 464, 689, and 947 nm shows that the strongest contributions (negative in the case of the negative signal at 464 nm and positive for the positive signals at 689 and 947 nm) come from hole states created in the occupied DOS in a narrow energy

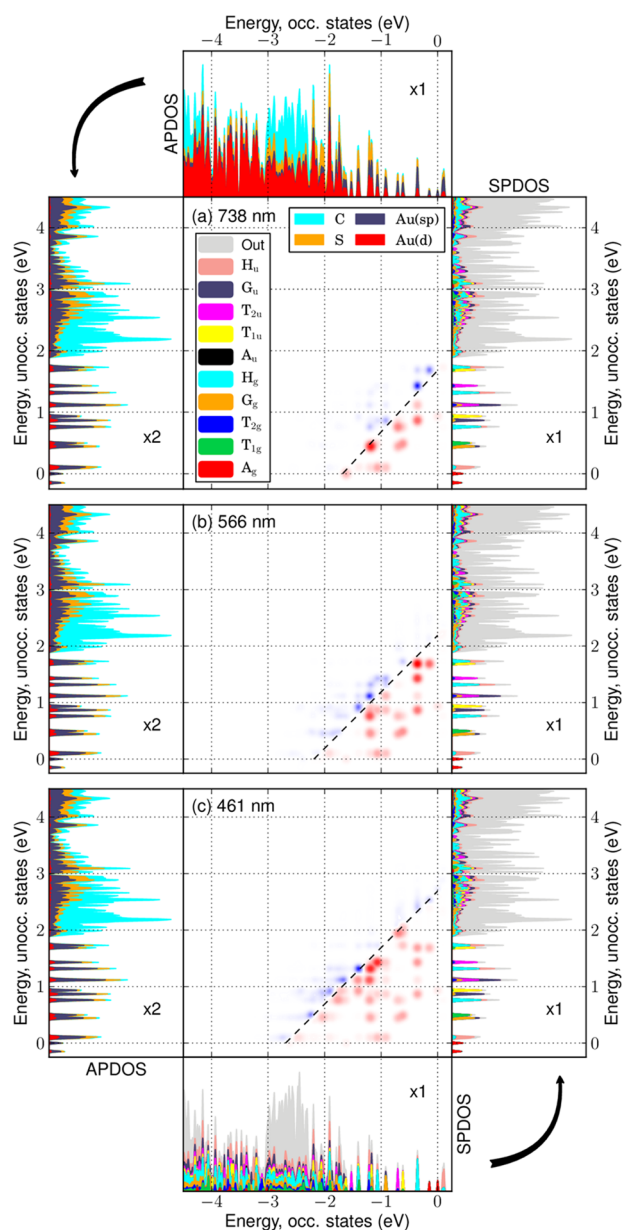


Figure 6. DTCM analysis of the three lowest-energy linear absorption peaks of $\text{Au}_{144}(\text{SCH}_2\text{Ph})_{60}$ as marked in Figure 4a. (a)–(c) at the center show single-particle contributions to the absorption at the given wavelength (energy). Red/blue contributions denote constructive/destructive contribution to the transition dipole. The brightness of the red/blue spots scales with the magnitude of contribution. The dashed diagonal lines denote the electron–hole (e–h) energy equaling the peak position, i.e., $\epsilon_e - \epsilon_h = hc/\lambda$. The electron states are formed in the manifold of the initially unoccupied states (right and left in (a)–(c)) and the hole states are formed in the manifold of the initially occupied states (top and bottom). The occupied–unoccupied electron density of states (DOS) is presented in two alternative ways. (Bottom right) Decomposition of the DOS projected to I_h symmetry representations (SPDOS); (top left) projection to spherical atomic orbitals (atom-projected APDOS). The Fermi energy is at zero.

range of $-1.5 \text{ eV} < \varepsilon < -1 \text{ eV}$ (Figure 8). These states are primarily located at the 60-atom Au layer and at the 30-unit SR–Au–SR layer at the interface between the gold nanocrystal and the ligand layer. Thus, the effect of the chiral metal–ligand

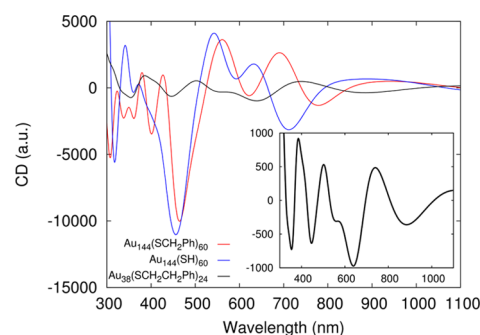


Figure 7. Computed CD absorption spectra for $\text{Au}_{144}(\text{SCH}_2\text{Ph})_{60}$ (red curve) and $\text{Au}_{144}(\text{SH})_{60}$ (blue curve) compared to the computed CD absorption spectrum of $\text{Au}_{38}(\text{SCH}_2\text{CH}_2\text{Ph})_{24}$ (black curve) taken from ref 52. The inset shows the $\text{Au}_{38}(\text{SCH}_2\text{CH}_2\text{Ph})_{24}$ data in a zoomed-in scale. Note in the y-scales: the strongest peaks in the $\text{Au}_{144}(\text{SR})_{60}$ spectra are almost 10 times higher than peaks at similar wavelengths in the $\text{Au}_{38}(\text{SR})_{24}$ spectrum. The magnitudes of the computed CD signals for all particles are directly comparable since the absorption cross sections show absolute values per one particle. The CD spectrum for $\text{Au}_{144}(\text{SCH}_2\text{Ph})_{60}$ and $\text{Au}_{144}(\text{SH})_{60}$ was calculated for the “right-handed” enantiomers shown in Figure 1a,c, where the arrangements of the five RS–Au–SR units around each C_5 axis form a “right-down” blade structure.

interface is directly manifested in the chiroptical behavior of $\text{Au}_{144}(\text{SCH}_2\text{Ph})_{60}$.

Comparison of I -Au₁₄₄(SR)₆₀ to C_1 -Au₁₄₄(SR)₄₀, C_{2v} -Au₁₄₆(SR)₅₇, and D_5 -Au₂₄₆(SR)₈₀. Two different gold nanoparticles, closely related in composition and size to Au₁₄₄(SR)₆₀, have been recently reported. Vergara et al. published⁴⁰ the X-ray crystal structure of Au₁₄₆(4MBA)₅₇ particle, and Azubel et al. reported⁴¹ the atomic structure of the 144-atom gold core of the 3MBA-protected particle, where the mass spectrometry yielded a low number (about 40) of ligands, hence the formulation of Au₁₄₄(3MBA)₄₀ (4MBA/3MBA is para/meta mercaptobenzoic acid, respectively). The Au₁₄₆(4MBA)₅₇ has a C_{2v} -symmetric, fcc-based metal core with one stacking fault while the core of Au₁₄₄(3MBA)₄₀ has only C_1 symmetry (see insets to Figure 9a,b). Since the count of metal-free electrons is similar to Au₁₄₄(SR)₆₀ particle, it is interesting to compare the details of the electronic structure and its implication to optical absorption between these systems. As Figure 9a,b shows, the computed optical absorption spectra of both of these lower-symmetry nanoparticles are qualitatively different from those of Au₁₄₄(SR)₆₀ (Figure 4), showing an otherwise monotonous increase in absorption with decreasing wavelength but a single weak absorption band at 520 nm for Au₁₄₄(3MBA)₄₀ and 443 nm for Au₁₄₆(4MBA)₅₇. The DTCM analysis for those energies reveals that the absorption band is caused by massive contributions from single e-h transitions from occupied states to unoccupied states within $E_F \pm 2.5$ eV. In general, transitions where $\epsilon_e - \epsilon_h < hc/\lambda$ contribute constructively to the absorption peak while transitions where $\epsilon_e - \epsilon_h > hc/\lambda$ contribute via screening. In the case of C_1 -symmetric Au₁₄₄(3MBA)₄₀, a separate constructive “diagonal band” by occupied and unoccupied states within $E_F \pm 1$ eV is formed, caused by the high dispersion of states close to E_F , in other words, by disappearance of the clear electronic shell structure.

Jin and collaborators reported⁶ in 2016 the crystal structure of a D_5 -symmetric $\text{Au}_{246}(\text{SPhCH}_3)_{80}$ nanoparticle, which, interestingly, did not show a plasmonic optical spectrum, but

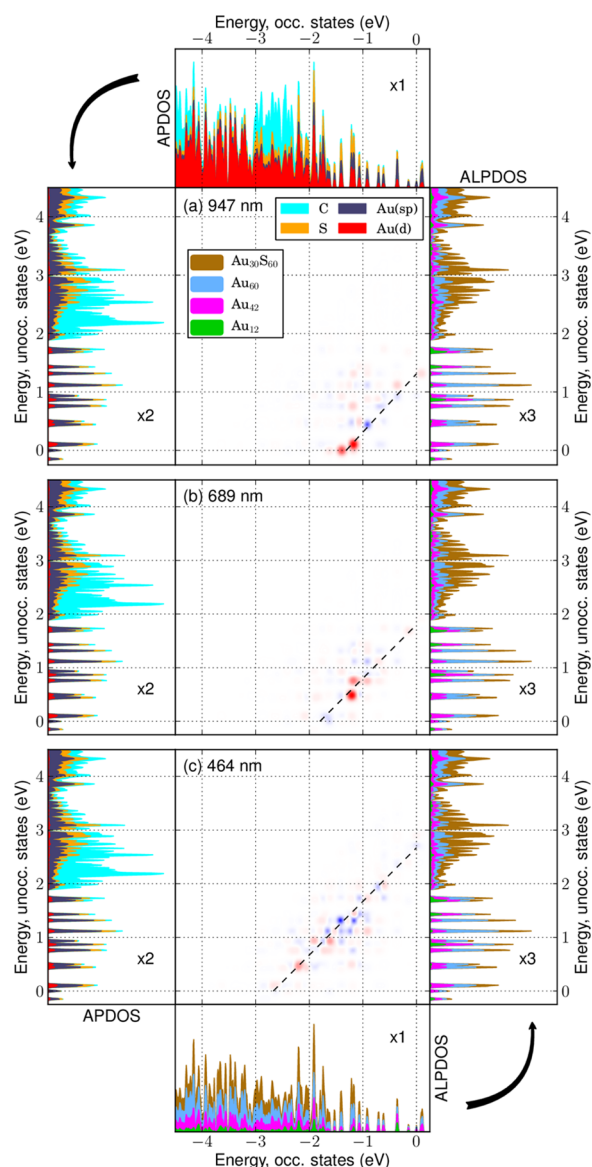


Figure 8. RTCM analysis of three selected peaks in the CD absorption spectrum of $\text{Au}_{144}(\text{SCH}_2\text{Ph})_{60}$ shown in Figure 7. The layout is similar to Figure 6, but here the red/blue spots denote constructive/destructive contributions to the rotational strengths. The single-electron DOS is presented either as projected to local atomic orbitals (APDOS, bottom and right) or by a layer-by-layer manner (ALPDOS, top and left). The dashed diagonal lines denote the electron–hole ($e-h$) energy equaling the peak position ($\varepsilon_e - \varepsilon_h = hc/\lambda$). The Fermi energy is at zero.

instead showed several distinguishable absorption bands similar to the $\text{Au}_{144}(\text{SR})_{60}$ case.⁵⁵ We analyzed here the electronic structure and optical absorption of the simplified model structure of $\text{Au}_{246}(\text{SH})_{80}$. As Figure 10 shows, the linear optical absorption curve shows five distinguishable bands for $\lambda > 400$ nm. The electronic structure of this nanoparticle shows that the states close to E_F are grouped to distinct shells according to D_5 symmetry representations,⁴⁵ and the DTCM analysis of the 432 nm band in Figure 9c shows that this shell structure leads to $e-h$ contributions to this band that are qualitatively much different from the smaller, low-symmetry particles in (a) and (b).

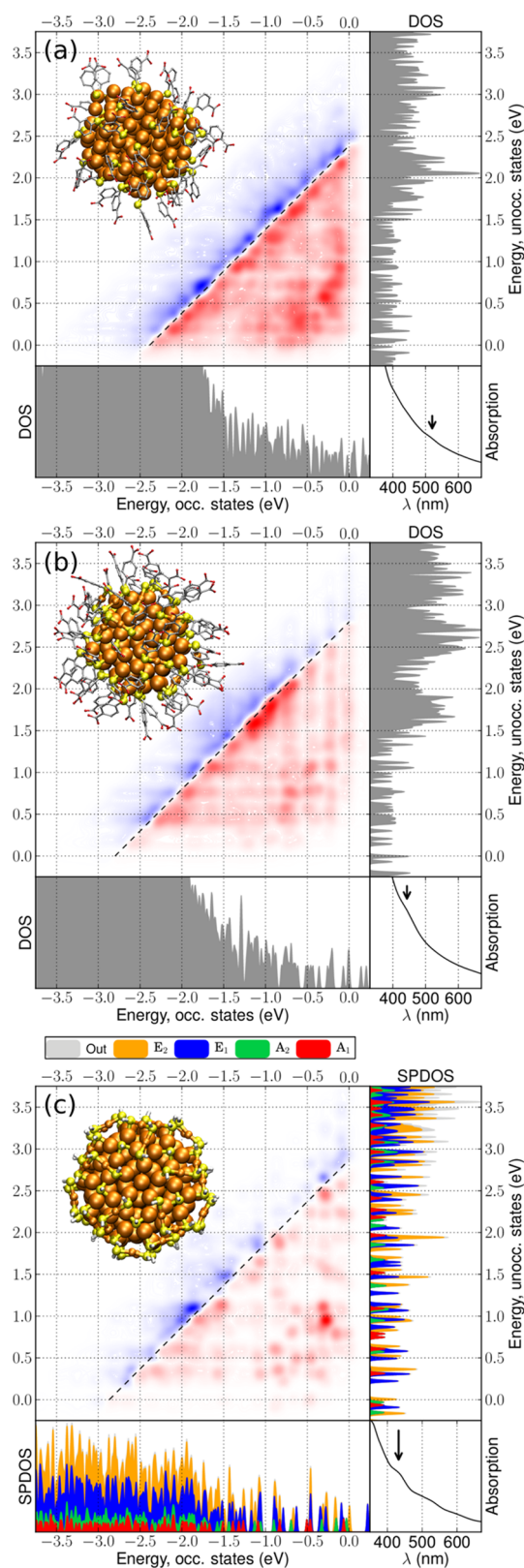


Figure 9. DTCM analysis of the computed linear absorption spectrum of (a) $\text{Au}_{144}(\text{3MBA})_{40}$, (b) $[\text{Au}_{146}(\text{4MBA})_{57}]^{3-}$, and (c) $\text{Au}_{246}(\text{SH})_{80}$, with nanoparticle structures shown as insets. (Bottom right) Computed absorption spectra, where the arrows show the analyzed absorption energy (520 nm in (a), 443 nm in (b), and 432 nm in (c)). The layout is otherwise similar to Figure 6, but the occupied and unoccupied electronic density of states (DOS) is shown in (a) and (b) without any symmetry assignments and with D_5

Figure 9. continued

representations in (c). The structures of the nanoparticles are shown as insets. The dashed diagonal lines denote the electron–hole (e–h) energy equaling the peak position ($\epsilon_e - \epsilon_h = hc/\lambda$). The Fermi energy is at zero. Note the qualitative changes in the density of electron states close to E_F when going from (a) to (c), with the DOS being most continuous in (a) and most peaked (to shells with well-defined D_5 representations) in (c).

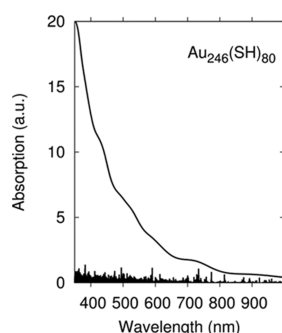


Figure 10. Computed linear optical absorption spectrum of $\text{Au}_{246}(\text{SH})_{80}$. The individual optical lines (marked by sticks) are broadened by 0.075 eV Gaussians for the continuous curves. Clear absorption bands are observed at 432, 516, 590, 713, and 897 nm, agreeing qualitatively well with the experiment on $\text{Au}_{246}(\text{SPhCH}_3)_{80}$.⁵⁵

CONCLUSIONS

In this work, we have systematically analyzed the electronic structure and optical properties of several recently reported gold nanoparticles between 144 and 246 gold atoms that are made by wet chemistry and whose structures have been resolved to atomic precision. This size region is important for understanding how the nanoparticles' properties change from molecular to metallic. We demonstrate the dominant role of the point group symmetry of the gold nanocrystal in determining the electronic shell structure of the particle, which in turn determines the details in the linear optical absorption spectrum as well as the grouping of the states close to the Fermi energy, defining the location and magnitude of the fundamental energy gap distinct for molecular particles. For particles of 144–146 gold atoms, the lower point group symmetry of the gold nanocrystal smears out the electronic shells creating a more continuous density of states close to E_F , a more monotonous linear optical absorption, and development of a single plasmon-like absorption band. Identification of clear electronic shell structure as projected to the D_5 symmetry of the $\text{Au}_{246}(\text{SR})_{80}$ explains the nonplasmonic absorption of this quite large nanoparticle that otherwise could be expected^{7,28} to be already plasmonic. Interestingly, silver nanoparticles have been predicted^{56,57} and observed^{58,59} to have plasmonic absorption at smaller sizes (136–141 silver atoms) than gold particles. This qualitative difference is likely to arise from different screening properties of the metal d-electrons due to the clearly different locations of the Ag(4d) and Au(5d) derived bands with respect to the Fermi energy of the nanoparticle. Finally, our work predicts that in the case of a successful enantioseparation of $\text{Au}_{144}(\text{SR})_{60}$, the handedness of the enantiopure particles can be undoubtedly recognized from the CD absorption spectrum facilitating their use in applications that require optical isomerism.

ASSOCIATED CONTENT

Supporting Information

The Supporting Information is available free of charge on the ACS Publications website at DOI: 10.1021/acs.jpcc.9b05863.

Visualization of the $\text{Au}_{144}(\text{SR})_{60}$ structure and additional analysis of the optical spectrum of $\text{Au}_{144}(\text{SH})_{60}$ (PDF)

AUTHOR INFORMATION

Corresponding Author

*E-mail: hannu.j.hakkinen@jyu.fi.

ORCID

Hannu Häkkinen: 0000-0002-8558-5436

Notes

The authors declare no competing financial interest.

ACKNOWLEDGMENTS

This work was supported by the Academy of Finland (grant 294217 and H.H.'s Academy Professorship). S.K. acknowledges the Väisälä Foundation for a Ph.D. study grant. Computations were made at the CSC supercomputer center in Espoo (Finland) and at the Barcelona supercomputing center (Spain) as part of the PRACE project NANOMETALS. The authors thank Z. Wu, I. Garzon, X. Lopez-Lozano, H. C. Weissker, A. Fortunelli, S. Vergara, R. L. Whetten, M. Azubel, and R. D. Kornberg for numerous discussions on the structure and properties of the $\text{Au}_{144}(\text{SR})_{60}$, $\text{Au}_{146}(\text{SR})_{57}$, and $\text{Au}_{144}(\text{SR})_{40}$ nanoparticles.

REFERENCES

- (1) Daniel, M. C.; Astruc, D. Gold Nanoparticles: Assembly, Supramolecular Chemistry, Quantum-Size-Related Properties, and Applications toward Biology, Catalysis, and Nanotechnology. *Chem. Rev.* **2004**, *104*, 293–346.
- (2) Boisselier, E.; Astruc, D. Gold Nanoparticles in Nanomedicine: Preparations, Imaging, Diagnostics, Therapies, and Toxicity. *Chem. Soc. Rev.* **2009**, *38*, 1759–1782.
- (3) Louis, C.; Pluchery, P. *Gold Nanoparticles for Physics, Chemistry and Biology*, 2nd ed.; World Scientific: London, 2017.
- (4) Faraday, M. The Bakerian Lecture: Experimental Relations of gold (and Other Metals) to Light. *Philos. Trans. R. Soc. London* **1857**, *147*, 145–181.
- (5) Tsukuda, T.; Häkkinen, H. *Protected Metal Clusters: From Fundamentals to Applications*; Elsevier: Amsterdam, 2015.
- (6) Zeng, C.; Chen, Y.; Kirschbaum, K.; Lambright, K. J.; Jin, R. Emergence of Hierarchical Structural Complexities in Nanoparticles and Their Assembly. *Science* **2016**, *354*, 1580–1584.
- (7) Sakthivel, N. A.; Theivendran, S.; Ganeshraj, V.; Oliver, A. G.; Dass, A. Crystal Structure of Faradaurate-279: $\text{Au}_{279}(\text{SR})_{84}$ Plasmonic Nanocrystal Molecules. *J. Am. Chem. Soc.* **2017**, *139*, 15450–15459.
- (8) Yan, J.; Malola, S.; Hu, C.; Peng, J.; Dittrich, B.; Teo, B. K.; Häkkinen, H.; Zheng, L.; Zheng, N. Co-Crystallization of Atomically Precise Metal Nanoparticles Driven by Magic Atomic and Electronic Shells. *Nat. Commun.* **2018**, *9*, No. 3357.
- (9) De Heer, W. A. The Physics of Simple Metal Clusters: Experimental Aspects and Simple Models. *Rev. Mod. Phys.* **1993**, *65*, 611–676.
- (10) Häkkinen, H. Atomic and Electronic Structure of Gold Clusters: Understanding Flakes, Cages and Superatoms from Simple Concepts. *Chem. Soc. Rev.* **2008**, *37*, 1847.
- (11) Walter, M.; Akola, J.; Lopez-Acevedo, O.; Jadzinsky, P. D.; Calero, G.; Ackerson, C. J.; Whetten, R. L.; Grönbeck, H.; Häkkinen, H. A Unified View of Ligand-Protected Gold Clusters as Superatom Complexes. *Proc. Natl. Acad. Sci. U.S.A.* **2008**, *105*, 9157–9162.

- (12) Häkkinen, H. Electronic Shell Structures in Bare and Protected Metal Nanoclusters. *Adv. Phys.: X* **2016**, *1*, 467–491.
- (13) Jena, P.; Sun, Q. Super Atomic Clusters: Design Rules and Potential for Building Blocks of Materials. *Chem. Soc. Rev.* **2018**, *118*, 5755–5870.
- (14) Fröhlich, H. Die Spezifische Wärme der Elektronen Kleiner Metallteilchen bei Tiefen Temperaturen. *Physica* **1937**, *4*, 406–412.
- (15) Kubo, R. Electronic Properties of Metallic Fine Particles I. *J. Phys. Soc. Jpn.* **1962**, *17*, 975–986.
- (16) Malola, S.; Häkkinen, H. How Many Gold Atoms Make Gold Metal? *Europhys. News* **2015**, *46*, 23–26.
- (17) Schaaff, T. G.; Shafigullin, M. N.; Khoury, J. T.; Vezmar, I.; Whetten, R. L. Properties of a Ubiquitous 29 kDa Au:SR Cluster Compound. *J. Phys. Chem. B* **2001**, *105*, 8785–8796.
- (18) Chaki, N. K.; Negishi, Y.; Tsunoyama, H.; Shichibu, Y.; Tsukuda, T. Ubiquitous 8 and 29 kDa Gold: Alkanethiolate Cluster Compounds: Mass-Spectrometric Determination of Molecular Formulas and Structural Implications. *J. Am. Chem. Soc.* **2008**, *130*, 8608–8610.
- (19) Qian, H.; Jin, R. Controlling Nanoparticles with Atomic Precision: The Case of Au144(SCH₂CH₂Ph)₆₀. *Nano Lett.* **2009**, *9*, 4083–4087.
- (20) Fields-Zinna, C.; Sardar, R.; Beasley, C. A.; Murray, R. W. Electrospray Ionization Mass Spectrometry of Intrinsically Cationized Nanoparticles (Au₁₄₄/146(SC₁₁H₂₂N(CH₂CH₃)₃)_x(S(CH₂-SCH₃)_y))_{x+}. *J. Am. Chem. Soc.* **2009**, *131*, 16266–16271.
- (21) Lopez-Acevedo, O.; Akola, J.; Whetten, R. L.; Grönbeck, H.; Häkkinen, H. Structure and Bonding in the Ubiquitous Icosahedral Metallic Gold Cluster Au₁₄₄(SR)₆₀. *J. Phys. Chem. C* **2009**, *113*, 5035–5038.
- (22) Ingram, R. S.; Hostetler, M. J.; Murray, R. W.; Schaaff, T. G.; Khoury, K.; Whetten, R. L.; Bigioni, T.; Guthrie, D. K.; First, P. N. 28 kDa Alkanethiolate-Protected Au Clusters Give Analogous Solution Electrochemistry and STM Coulomb Staircases. *J. Am. Chem. Soc.* **1997**, *119*, 9279–9280.
- (23) Hicks, J. F.; Miles, D. T.; Murray, R. W. Quantized Double-Layer Charging of Highly Monodisperse Metal Nanoparticles. *J. Am. Chem. Soc.* **2002**, *124*, 13322–13328.
- (24) Quinn, B. M.; Liljeroth, P.; Ruiz, V.; Laaksonen, T.; Kontturi, K. Electrochemical Resolution of 15 Oxidation States for Monolayer Protected Gold Nanoparticles. *J. Am. Chem. Soc.* **2003**, *125*, 6644–6645.
- (25) Salorinne, K.; Lahtinen, T.; Koivisto, J.; Kalenius, E.; Nissinen, M.; Pettersson, M.; Häkkinen, H. Nondestructive Size Determination of Thiol-Stabilized Gold Nanoclusters in Solution by Diffusion Ordered NMR Spectroscopy. *Anal. Chem.* **2013**, *85*, 3489–3492.
- (26) Yi, C.; Tofanelli, M. A.; Ackerson, C. J.; Knappenberger, K., Jr. Optical Properties and Electronic Energy Relaxation of Metallic Au₁₄₄(SR)₆₀ Nanoclusters. *J. Am. Chem. Soc.* **2013**, *135*, 18222–18228.
- (27) Koivisto, J.; Salorinne, K.; Mustalahti, S.; Lahtinen, T.; Malola, S.; Häkkinen, H.; Pettersson, M. Vibrational Perturbations and Ligand-Layer Coupling in a Single Crystal of Au₁₄₄(SC₂H₄Ph)₆₀ Nanocluster. *J. Phys. Chem. Lett.* **2014**, *5*, 387–392.
- (28) Negishi, Y.; Nakazaki, T.; Malola, S.; Takano, S.; Niihori, Y.; Kurashige, W.; Yamazoe, S.; Tsukuda, T.; Häkkinen, H. A Critical Size for Emergence of Nonbulk Electronic and Geometric Structures in Dodecanethiolate-Protected Au Clusters. *J. Am. Chem. Soc.* **2015**, *137*, 1206–1212.
- (29) Weissker, H. C.; Escobar, H. B.; Thanthirige, V. D.; Kwack, K.; Lee, D.; Ramakrishna, G.; Whetten, R. L.; Lopez-Lozano, X. Information on Quantum States Pervades the Visible Spectrum of the Ubiquitous Au₁₄₄(SR)₆₀ Gold Nanocluster. *Nat. Commun.* **2014**, *5*, No. 3785.
- (30) Weissker, H. C.; Lopez-Acevedo, O.; Whetten, R. L.; Lopez-Lozano, X. Optical Spectra of the Special Au₁₄₄ Gold-Cluster Compounds: Sensitivity to Structure and Symmetry. *J. Phys. Chem. C* **2015**, *119*, 11250–11259.
- (31) Kumara, C.; Dass, A. (AuAg)₁₄₄(SR)₆₀ Alloy Nanomolecules. *Nanoscale* **2011**, *3*, 3064–3067.
- (32) Malola, S.; Häkkinen, H. Electronic Structure and Bonding of Icosahedral Core–Shell Gold–Silver Nanoalloy Clusters Au₁₄₄–xAg_x(SR)₆₀. *J. Phys. Chem. Lett.* **2011**, *2*, 2316–2321.
- (33) Malola, S.; Lehtovaara, L.; Häkkinen, H. TDDFT Analysis of Optical Properties of Thiol Monolayer-Protected Gold and Intermetallic Silver–Gold Au₁₄₄(SR)₆₀ and Au₈₄Ag₆₀(SR)₆₀ Clusters. *J. Phys. Chem. C* **2014**, *118*, 20002–20008.
- (34) Dharmaratne, A. C.; Dass, A. Au₁₄₄–xCu_x(SC₆H₁₃)₆₀ Nanomolecules: Effect of Cu Incorporation on Composition and Plasmon-Like Peak Emergence in Optical Spectra. *Chem Commun.* **2014**, *50*, 1722.
- (35) Malola, S.; Hartmann, M. J.; Häkkinen, H. Copper Induces a Core Plasmon in Intermetallic Au (144,145)–xCu_x(SR)₆₀ Nanoclusters. *J. Phys. Chem. Lett.* **2015**, *6*, 515–520.
- (36) Wong, O. A.; Heinecke, C. L.; Simone, A. R.; Whetten, R. L.; Ackerson, C. J. Ligand-Symmetry-Equivalence on Thiolate Protected Gold Nanoclusters Determined by NMR Spectroscopy. *Nanoscale* **2012**, *4*, 4099–4102.
- (37) Guryanov, I.; Polo, F.; Ubyvovk, E. V.; Korzhikova-Vlakh, E.; Tennikova, T.; Rad, A. T.; Nieh, M. P.; Maran, F. Polylysine-Grafted Au₁₄₄ Nanoclusters: Birth and Growth of a Healthy Surface-Plasmon-Resonance-Like Band. *Chem. Sci.* **2017**, *8*, 3228–3238.
- (38) Lei, Z.; Li, J. J.; Wang, X. K.; Zhang, W. H.; Wang, Q. M. Isolation and Total Structure Determination of an All Alkynyl-Protected Gold Nanocluster Au₁₄₄. *Angew. Chem., Int. Ed.* **2018**, *57*, 8639–8643.
- (39) Yan, N.; Xia, N.; Liao, L.; Zhu, M.; Jin, F.; Jin, R.; Wu, Z. Unravelling the Long-Pursued Au₁₄₄ Structure by X-ray Crystallography. *Sci. Adv.* **2018**, *4*, No. eaat7259.
- (40) Vergara, S.; Lukes, D. A.; Martynowycz, M. W.; Santiago, U.; Plascencia-Villa, G.; Weiss, S. C.; de la Cruz, M. J.; Black, D. M.; Alvarez, M. M.; Lopez-Lozano, X.; et al. MicroED Structure of Au₁₄₆(pMBA)₅₇ at Subatomic Resolution Reveals a Twinned FCC Cluster. *J. Phys. Chem. Lett.* **2017**, *8*, 5523–5530.
- (41) Azubel, M.; Koh, A. L.; Koyasu, L.; Tsukuda, T.; Kornberg, R. D. Structure Determination of a Water-Soluble 144-Gold Atom Particle at Atomic Resolution by Aberration-Corrected Electron Microscopy. *ACS Nano* **2017**, *11*, 11866–11871.
- (42) Tero, T. R.; Malola, S.; Koncz, B.; Pohjolainen, E.; Lautala, S.; Mustalahti, S.; Permi, P.; Groenhof, G.; Pettersson, M.; Häkkinen, H. Dynamic Stabilization of the Ligand-Metal Interface in Atomically Precise Gold Nanoclusters Au₆₈ and Au₁₄₄ Protected by Mercaptobenzoic Acid. *ACS Nano* **2017**, *11*, 11872–11879.
- (43) Enkovaara, J.; Rostgaard, C.; Mortensen, J. J.; Chen, J.; Dulak, M.; Ferrighi, L.; Gavnholt, J.; Glinvald, C.; Haikola, V.; Hansen, A.; et al. Electronic Structure Calculations with GPAW: A Real-Space Implementation of the Projector Augmented-Wave Method. *J. Phys.: Condens. Matter* **2010**, *22*, No. 253202.
- (44) Perdew, J. P.; Burke, K.; Ernzerhof, M. Generalized Gradient Approximation Made Simple. *Phys. Rev. Lett.* **1996**, *77*, 3865–3868.
- (45) Kaappa, S.; Malola, S.; Häkkinen, H. Point Group Symmetry Analysis of the Electronic Structure of Bare and Protected Metal Nanocrystals. *J. Phys. Chem. A* **2018**, *122*, 8576–8584.
- (46) Walter, M.; Häkkinen, H.; Lehtovaara, L.; Puska, M.; Enkovaara, J.; Rostgaard, C.; Mortensen, J. J. Time-Dependent Density-Functional Theory in the Projector Augmented-Wave Method. *J. Chem. Phys.* **2008**, *128*, No. 244101.
- (47) Malola, S.; Lehtovaara, L.; Enkovaara, J.; Häkkinen, H. Birth of the Localized Surface Plasmon Resonance in Monolayer-Protected Gold Nanoclusters. *ACS Nano* **2013**, *7*, 10263–10270.
- (48) Deng, G.; Malola, S.; Yan, J.; Han, Y.; Yuan, P.; Zhao, C.; Yuan, X.; Lin, S.; Tang, Z.; Teo, B. K.; et al. From Symmetry Breaking to Unraveling the Origin of the Chirality of Ligated Au₁₃Cu₂ clusters. *Angew. Chem., Int. Ed.* **2018**, *57*, 3421–3425.
- (49) Martin, T. P.; Bergmann, T.; Göhlich, H.; Lange, T. Shell Structure of Clusters. *J. Phys. Chem. A* **1991**, *95*, 6421–6429.

- (50) Häkkinen, H. The Gold-Sulfur Interface at the Nanoscale. *Nat. Chem.* **2012**, *4*, 443–455.
- (51) Zhang, B.; Kaziz, S.; Li, H.; Wodka, D.; Malola, S.; Safonova, O.; Nachtegaal, M.; Mazet, C.; Dolamic, I.; Llorca, J.; et al. Pd₂Au₃₆(SR)₂₄ Cluster: Structural Studies. *Nanoscale* **2015**, *7*, 17012–17019.
- (52) Lopez-Acevedo, O.; Tsunoyama, H.; Tsukuda, T.; Häkkinen, H.; Aikens, C. M. Chirality and Electronic Structure of the Thiolate-Protected Au₃₈ Nanocluster. *J. Am. Chem. Soc.* **2010**, *132*, 8210–8218.
- (53) Qian, H.; Eckenhoff, W. T.; Zhu, Y.; Pintauer, T.; Jin, R. Total Structure Determination of Thiolate-Protected Au₃₈ Nanoparticles. *J. Am. Chem. Soc.* **2010**, *132*, 8280–8281.
- (54) Dolamic, I.; Knoppe, S.; Dass, A.; Buergi, T. First Enantioseparation and Circular Dichroism Spectra of Au₃₈ Clusters Protected by Achiral Ligands. *Nat. Commun.* **2012**, *3*, No. 798.
- (55) Zhou, M.; Zeng, C. J.; Song, Y. B.; Padelford, J. W.; Wang, G. L.; Sfeir, M. Y.; Higaki, T.; Jin, R. C. On the Non-Metallicity of 2.2 nm Au₂₄₆(SR)₈₀ Nanoclusters. *Angew. Chem., Int. Ed.* **2017**, *56*, 16257–16261.
- (56) Guidez, E. B.; Aikens, C. M. Quantum Mechanical Origin of the Plasmon: From Molecular Systems to Nanoparticles. *Nanoscale* **2014**, *6*, 11512–11527.
- (57) Kuisma, M.; Sakko, A.; Rossi, T. P.; Larsen, A. H.; Enkovaara, J.; Lehtovaara, L.; Rantala, T. T. Localized Surface Plasmon Resonance in Silver Nanoparticles: Atomistic First-Principles Time-Dependent Density-Functional Theory Calculations. *Phys. Rev. B* **2015**, *91*, No. 115431.
- (58) Yang, H.; Wang, Y.; Chen, X.; Zhao, X.; Gu, L.; Huang, H.; Yan, J.; Xu, C.; Li, G.; Wu, J.; et al. Plasmonic Twinned Silver Nanoparticles with Molecular Precision. *Nat. Commun.* **2016**, *7*, No. 12809.
- (59) Ren, L. T.; Yuan, P.; Su, H. F.; Malola, S.; Lin, S. C.; Tang, Z. C.; Teo, B. K.; Häkkinen, H.; Zheng, L. S.; Zheng, N. Bulky Surface Ligands Promote Surface Reactivities of [Ag₁₄₁X₁₂(S-Adm)₄₀]³⁺ (X = Cl, Br, I) Nanoclusters: Models for Multiple-Twinned Nanoparticles. *J. Am. Chem. Soc.* **2017**, *139*, 13288–13291.